nature communications

Article

https://doi.org/10.1038/s41467-025-57069-1

Organelle-like structural evolution of coacervate droplets induced by photopolymerization

Received: 28 July 2024

Accepted: 11 February 2025

Published online: 20 February 2025

Check for updates

Mei Zhu, Zhenhui Li, Junbo Li, Youping Lin, Haixu Chen, Xin Qiao, Xiaoliang Wang, Xiaoman Liu & Xin Huang

The dynamic study of coacervates in vitro contributes our understanding of phase separation mechanisms in cells due to complex intracellular physiology. However, current researches mainly involve the use of exogenous auxiliary agents to form multi-compartmental coacervates with short-term stability. Herein, we report the endogenous self-organizing of multi-component coacervates (HA/PDDA/BSA/DMAEMA) induced by a dynamic stimulation process of protein-mediated photopolymerization. As polymerization proceeds, the cycled structural evolution and maturation from coacervate droplets into multi-compartmental coacervates, coacervate vesicles and coacervate droplets are revealed, which are driven by electrostatic interaction and osmotic pressure difference supported by dynamic and thermodynamic control. Specially, by regulating the light stimulation time, a type of multi-compartmental coacervates can be widely obtained with high structural stability over 300 days. Being a promising artificial cell model, it shows the special characteristic of compartmentalized encapsulation of substrates, efficiently improving enzymatic interfacial catalytic efficiency of organelle-like communication. Our study holds great potential for advancing the understanding of the structural evolution mechanism of membraneless organelles and provides an instructive technique for constructing multi-compartmental coacervates with long-term stability.

The coacervate droplets formed by liquid–liquid phase separation regarded as a promising protocell model[1–4] give rise to cell-like behaviors[5–9]. The coacervate droplets, with characteristics of molecularly crowded interior and spontaneous capture of substances, effectively promote the efficiency of intercellular biomolecular synthesis[10], storage catalysis[11–14], and living material assembly construction[15], etc. Due to the tendency of coacervate coalescence, some studies have focused on the membranization of coacervates for stability and functionalization purposes[16–22]. Furthermore, complex coacervates involving phase transitions are investigated[23–25], and the organization rules of multiphase coacervates are also revealed by learning the assembly of different property components[26–28].

Membraneless organelles involving phase separation mechanism are ubiquitous in cells, such as nucleolus[29], Cajal body[30] and stress granules[31], and many physiological activities also involve phase separation processes, such as neuroblast asymmetric division[32], autophagic degradation[33], innate immune signaling[34], etc. The complex physiological reactions are very common within cells[35], and the dynamic process is closely related to intracellular liquid-liquid phase separation. In the cell cycle, the nucleolus is a highly dynamic structure that exhibits periodic disappearance and reconstruction during

MIIT Key Laboratory of Critical Materials Technology for New Energy Conversion and Storage, School of Chemistry and Chemical Engineering, Harbin Institute of Technology, Harbin 150001, P. R. China. e-mail: liuxiaoman@hit.edu.cn; xinhuang@hit.edu.cn

mitosis. Cajal body generally undergoes disassembly in the mitotic period, and its reassembly is related to the gene transcription level and the proliferation rate of cells. Stress granules, as a temporary shelter for mRNA and proteins, will rapidly form inside cells when cells are stimulated by high temperature, oxidative stress, and irradiation, etc. After the disappearance of environmental stress, the stress granules dissociate again. These membraneless organelles exhibit dynamic transformation processes. Currently, many studies have shown that the sustained and abnormal formation of stress granules is associated with neurodegenerative diseases, revealing that the aggregation and precipitation of disease proteins in stress granules are important pathogenic mechanisms of various neurodegenerative diseases[36]. However, other studies have also demonstrated that the relationship between phase separation and pathogenic mechanisms does not always involve protein precipitation. For example, when motor neurons are subjected to adverse environmental stimuli, mutant protein Glycyl-tRNA synthetase (GlyRS), leading to Charcot-Marie-Tooth type 2 neuropathies (CMT2D), interacts with core protein G3BP of stress granules. Outwardly, the aberrant G3BP interaction does not affect the dynamic assembly and disassembly of stress granules, nor does it produce the protein precipitation. However, the abnormal interaction can significantly interfere with the protein network of stress granules, and a large amount of residual non-stress particle components disrupt the normal stress response of cells. By breaking the abnormal combination, the disease symptoms of the CMT2D mouse model can be effectively alleviated[37]. Therefore, the impact of phase separation on cellular function is not only related to the molecular structure of proteins such as multivalent domains[38] or intrinsically disordered regions (IDRs)[39], but also related to the dynamic transformation process of phase separation assemblies.

A kinetic process is usually accompanied by fast composition changes, leading to the generation of osmotic pressure, which contradicts the tight internal structure and liquid-like mobility of coacervates. To date, the implementation of non-equilibrium dynamic process of coacervates generally requires the auxiliary agents to stabilize at the surface of coacervates[40,41] or depends on the temperature sensitive[41,42] or charged components[43–45] of the coacervate. The dynamic transform of coacervates based on chemical reactions and the relationship between the transient states of non-equilibrium and thermodynamically stable structures have received minimal attention.

When cells are subjected to external stimuli, membraneless organelles play a crucial role in maintaining cellular physiological processes, and generally have a high protein density. Herein, from the perspective of protein functionality, we attempt to explore the relationship between the functional response of proteins and the dynamic transformation of membraneless organelles upon exposure to irradiation stimulation. That will further reveal the structural transition process of membraneless organelles and the relevance between dynamic non-equilibrium states and thermodynamic equilibrium structures of membraneless organelles, which may provide a perspective for researching on the pathogenic mechanisms of cells.

Given that multivalent interactions are the main driving force for the intracellular liquid-liquid phase separation, in this study, we demonstrate a type of dynamic-driven self-organization process of multi-componental coacervates composed of polysaccharides, proteins, and polymers by employing the protein-mediated photopolymerization under light stimulation[46], in which the structural evolution couples with endogenous homeostatic multi-compartmental coacervates amidst changing environmental conditions. To explore the dynamic process of coacervate droplets, the counter-charged poly dimethyl diallyl ammonium chloride (PDDA, Mw 200–350 kDa) and hyaluronic acid (HA, Mw ~50 kDa) coacervates are firstly formed, followed by adding bovine serum albumin (BSA) and methacrylic acid 2-(dimethylamino) ethyl ester (DMAEMA) monomers. Under light stimuli, BSA is activated to mediate the chain propagation reaction of DMAEMA within the coacervates, resulting in formation of the multi-compartmental coacervates via the mechanisms of osmotic pressure balance and electrostatic interaction. The multi-compartmental coacervates display excellent compartmental encapsulation features that various dyes/proteins are separated in the matrix or sub-compartments, respectively, and show efficient interfacial catalysis of lipases. Specially, as the polymerization reaction proceeds, the dynamic process is revealed that the homogeneous coacervates transform into the multi-compartmental coacervates and coacervate vesicles. Furthermore, the coacervate vesicles can spontaneously turn into spherical homogeneous coacervate supported by thermodynamic control. After 180 days, the multi-compartmental coacervates still show the separated encapsulation of dyes. Even after being placed over 300 days, the homogeneous catalysis of multi-compartmental coacervates could be realized, exhibiting enhanced catalytic efficiency (Fig. 1 and Supplementary Fig. 1a).

Results

Formation of multi-compartmental coacervates

The HA/PDDA coacervates were first constructed at the volume ratio of HA/PDDA = 3:1 (HA = 15 mg/mL, PDDA = 85 mg/mL) based on electrostatic interaction (> 400 mM NaCl, complete dissociation) (Fig. 2a and Supplementary Figs. 1b–g, 2), and the coacervates were stable within a wide pH range of 2-12 (Supplementary Fig. 3). By adding BSA (7.5 mg/mL) and DMAEMA (5% w/v), the HA/PDDA/BSA/DMAEMA complex coacervate droplets could be widely formed with homogeneous interior (Fig. 2b and Supplementary Figs. 4, 5). The coacervates with molecularly crowded interiors can spontaneously take up negative dyes (calcein, fluorescein sodium) while excluding positive dyes (RBITC, Rhodamine B), hydrophobic dye (Nile red) and dextran-FITC with a molecular weight over 40 kDa (Supplementary Fig. 6). By labeling BSA with FITC (BSA-FITC, green fluorescence), the CLSM images indicated that DMAEMA can facilitate the encapsulation of BSA into the coacervates (Fig. 2c, d and Supplementary Fig. 7). Subsequently, under 405 nm illumination with anaerobic ambiance, BSA-mediated photopolymerization could be carried out in the coacervate droplets. Then, the generated polymer (PDMAEMA) can induce the formation of multi-compartmental coacervates, which showed excellent compartmental sequestration on dyes. Calcein (green fluorescence) was sequestrated in the coacervate matrix, while Nile red (red fluorescence) was encapsulated in sub-compartments (Fig. 2e and Supplementary Figs. 8, 9). The SEM image revealed the obvious chamber of the multi-compartmental coacervates (Fig. 2f), and the three-dimensional CLSM image also showed the characteristic of compartmentalization (Fig. 2g). As a control experiment, in the absence of illumination or anaerobic conditions, no multi-compartmental coacervates was observed and the coacervates dissociated, indicating that BSA-mediated photopolymerization was necessary for the formation of multi-compartmental structures (Supplementary Fig. 10).

Bleaching was performed at different positions of the multi-compartmental coacervates, marked as 1 or 2, located at the connections of tow/multiple sub-compartments, respectively. The corresponding fluorescent recovery plots revealed that the fluorescence of both recovered within 20 s (Fig. 2h, i, and Supplementary Fig. 11), suggesting that the multi-compartmental coacervates still maintained fine mobility resembling the original coacervates (0 h). Besides, by further assessment of compartmental encapsulation of multi-compartmental coacervates, we found that the matrix of multi-compartmental coacervate showed the similar encapsulation behavior to that of the original coacervates. The negative dyes (calcein, fluorescein sodium) were preferentially sequestered into the matrix, while dextran-FITC with a molecular weight over 40 kDa was excluded. Significantly, the multi-compartmental coacervate exhibited specific encapsulation for hydrophobic dye Nile red, positive dyes RBITC and rhodamine B within sub-compartments (Supplementary Fig. 12).

https://doi.org/10.1038/s41467-025-57069-1

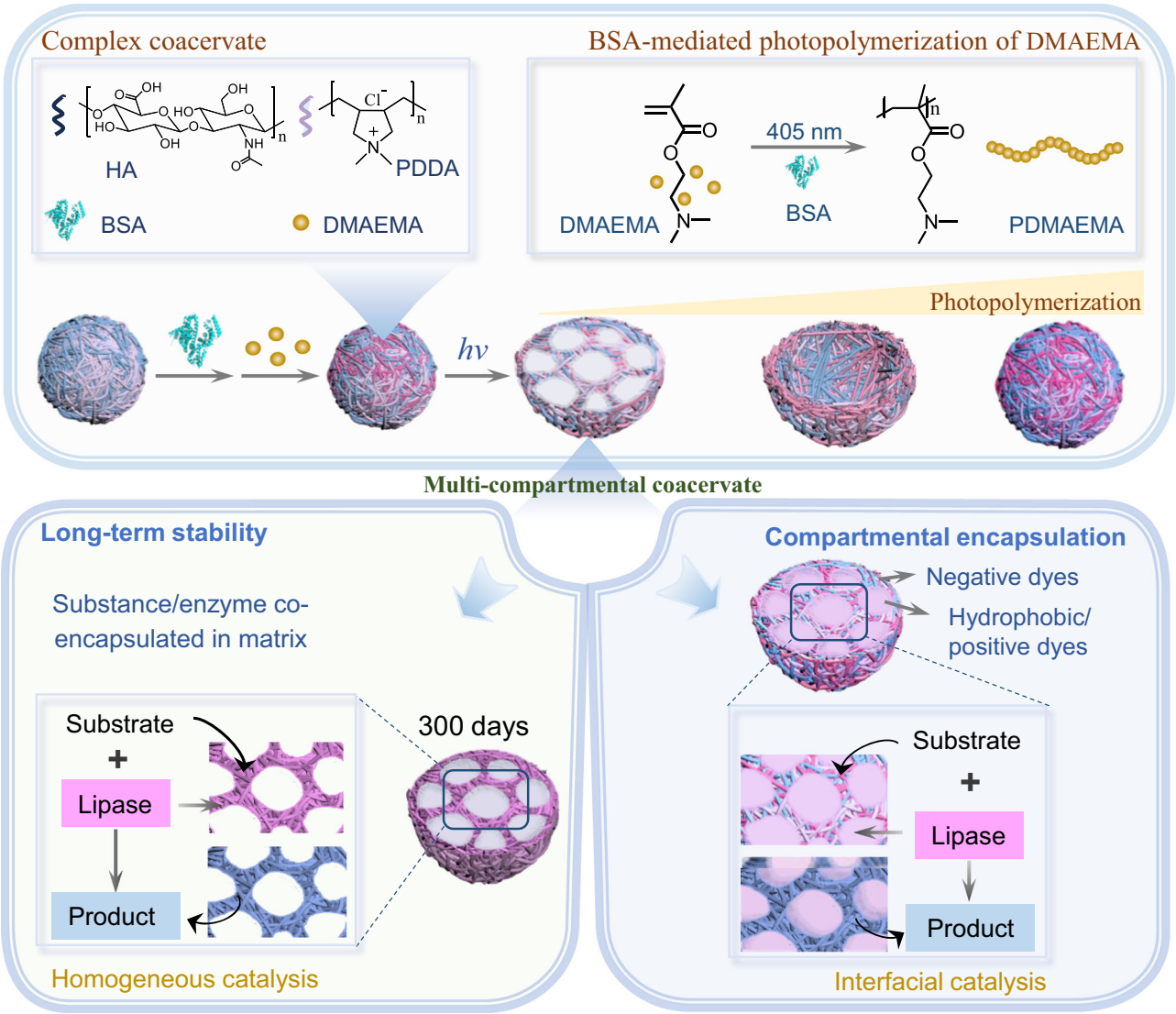

Fig. 1 | Schematic illustration of the formation of multi-compartmental coacervates and the dynamic structural transformation of coacervate droplets induced by BSA-mediated photopolymerization. Specially, the formed multi-compartmental coacervates show long-term stability with enhanced interfacial catalytic efficiency of lipases.

To further elucidate spatial composition of multi-compartmental coacervates, we specially synthesized positively charged polymer PMAEB labeled by RBITC (poly ethyl bromide salt of dimethylaminoethyl methacrylate) in place of PDDA to form HA/PMAEB/BSA/DMAEMA coacervates, and the HA/PMAEB/BSA/DMAEMA multi-compartmental coacervate was also successfully constructed (Supplementary Figs. 13–15). Through adding HA labeled with 5-aminofluorescein (HA-AF) and BSA labeled with FITC (BSA-FITC), respectively, the results revealed that the components, including PMAEB-RBITC (red), HA-AF (green), and BSA-FITC (green) were mainly distributed in the coacervate matrix (Fig. 2j). The generation of PDMAEMA triggered the formation of the multi-compartments, which increased the zeta potential of the coacervate solution towards a positive potential (Supplementary Fig. 16). We further explored the spatial distribution of PDMAEMA. The fluorescent PDMAEMA was synthesized by labeling with fluorescein O-methacrylate (PDMAEMA-FMA, green fluorescence), and mixed in the order of PDDA, PDMAEMA, HA, and BSA. PDMAEMA-FMA was mainly located at the surface of coacervates phase (Fig. 2j and Supplementary Fig. 17). To extend our exploration of PDMAEMA distribution, the coacervate solution after polymerization for 2.5 h was centrifuged and then discarded the supernatant, followed by immediately resuspending in H_2O. The multi-compartmental coacervates exhibited a high zeta potential of about 59.7 ± 1.2 mV. The resuspended multi-compartmental coacervates in H_2O were stained with RBITC (red) and calcein (green). As a result, RBITC was located at the external and internal interfaces, separated by a central green region stained with calcein (Fig. 2k). This observation also suggested that PDMAEMA could be preferentially coated at internal and external interface of the multi-compartmental coacervates, leading to an increase in zeta potential of the coacervate phase, based on electrostatic interaction between BSA and PDMAEMA (Supplementary Fig. 18 and Fig. 2l).

Multi-compartmental coacervates induced by photopolymerization

With the happening of polymerization, the generated PDMAEMA inside the coacervate droplets could increase the electrostatic interaction of the coacervate, which drives the external aqueous influx into the interior to form the multi-compartmental structure. To elucidate the formation mechanism of multi-compartments, the interior of HA/PDDA/BSA/DMAEMA coacervates containing calcein and RBITC dyes was locally irradiated by 488 nm laser. CLSM images clearly showed

https://doi.org/10.1038/s41467-025-57069-1

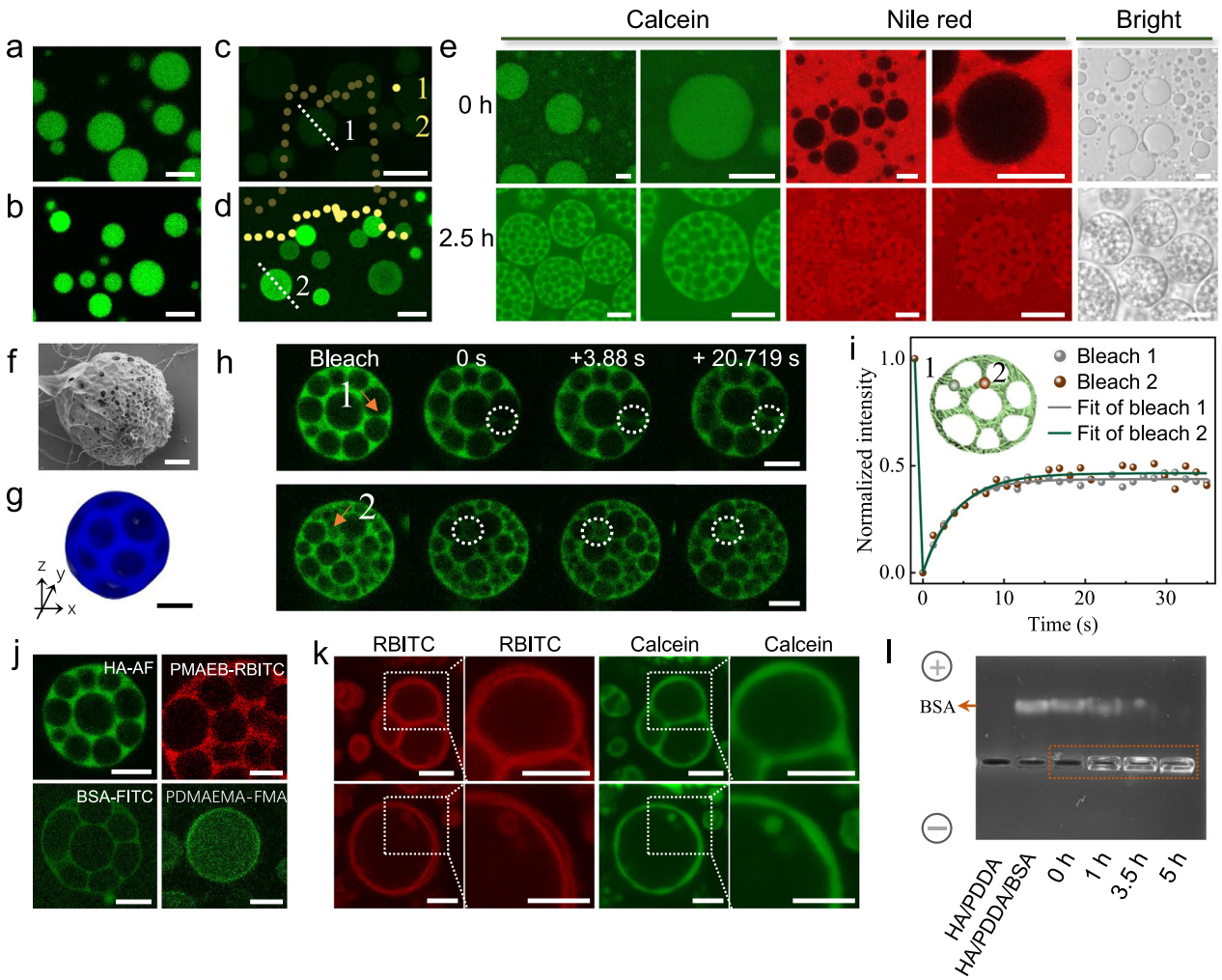

Fig. 2 | Dynamic formation of multi-compartmental coacervates induced by photopolymerization. CLSM images of coacervates with different components: (**a**) HA/PDDA, (**b**) HA/PDDA/BSA, HA labeled by 5-aminofluorescein named HA-AF (green). CLSM images of the spatial distributions of BSA (labeled by FITC, green) in (**c**) HA/PDDA/BSA coacervates and (**d**) HA/PDDA/BSA/DMAEMA coacervates, observed at 10 min and 1 min, respectively. The short dot lines are the corresponding line fluorescence intensity shown in (**c**, **d**), showing that DMAEMA facilitates the encapsulation of BSA into the coacervates. **e** CLSM images of HA/PDDA/BSA/DMAEMA coacervates under 405 nm illumination at 0 h and 2.5 h. The formed multi-compartmental droplets show that calcein (green) is sequestrated in the coacervate matrix, while Nile red (red) is encapsulated in sub-compartments. **f** SEM image of the multi-compartmental coacervates after vacuum freeze drying. **g** Three-dimensional image of a single multi-compartmental coacervate (Fluorescamine, blue). **h** CLSM images of the multi-compartmental coacervate bleached at different positions marked with 1 and 2 during a FRAP experiment, (HA-AF, green). **i** Corresponding fluorescent recovery plots in (**h**). The multi-compartmental coacervates (HA/PDDA/BSA/DMAEMA) are formed by 405 nm illumination for 2.5 h in (**e**–**i**). **j** Spatial distribution of multi-compartmental coacervate components including HA, PMAEB, BSA and PDMEMA, labeled by different fluorescent dyes, respectively. Scale bars in (**a**–**j**), 5 μm. **k** CLSM images of the resuspended multi-compartmental coacervates in H_2O after centrifugation, showing that RBITC (red) is encapsulated in the inner and the outer membrane while calcein (green) is sequestrated in the coacervate matrix. The multi-compartmental coacervates are formed by 405 nm illumination for 5 h. Scale bars in (**k**), 3 μm. **l** Agarose gel electrophoresis of HA/PDDA coacervates, HA/PDDA/BSA coacervates, HA/PDDA/BSA/DMAEMA coacervates (0 h) and multi-compartmental coacervates formed by illumination under 405 nm for 1 h, 3.5 h and 5 h, respectively. Running time, 70 min. The concentration of BSA decreases, while the brightness of the bands marked in the orange box increases and the bands tend to move towards a negative direction, suggesting an increase in the concentration of positive PDMAEMA and the interaction between BSA and PDMAEMA. Source data are provided as a Source Data file.

the ingress of external solution along with the uptake of RBITC, which indicated that the internal driving force facilitated the generation of multiple vacuoles (Supplementary Figs. 19, 20). When the multi-compartmental coacervate droplets were centrifuged and then resuspended in H_2O, it was clearly observed that fusion between the sub-compartments occurred with the ingress of H_2O into the coacervate droplets (Supplementary Fig. 21). The results indicated that the internal and external osmotic pressure balance is an important factor to keep multi-compartmental coacervates stable. When the multi-compartmental coacervate was exposed to high concentration salt solution, the multi-compartmental coacervates dissociated (Supplementary Fig. 22). Moreover, the content of the monomer in the coacervates phase and bulk solution was investigated, and the conversion ratio of DMAEMA was determined by ^{1}H NMR. It was found that the concentration of DMAEMA in the supernatant decreased over polymerization time, which would lead to a reduced osmotic pressure of the external solution. Decreasing osmotic pressure of bulk solution is beneficial for the formation of the internal sub-compartments. (Supplementary Figs. 23–25).

Dynamic structural evolution of coacervate droplets

Based on the above observations, by elongating the polymerization time, with the accumulation of PDMAEMA inside the coacervates, more dynamic evolution processes of multi-compartmental

https://doi.org/10.1038/s41467-025-57069-1

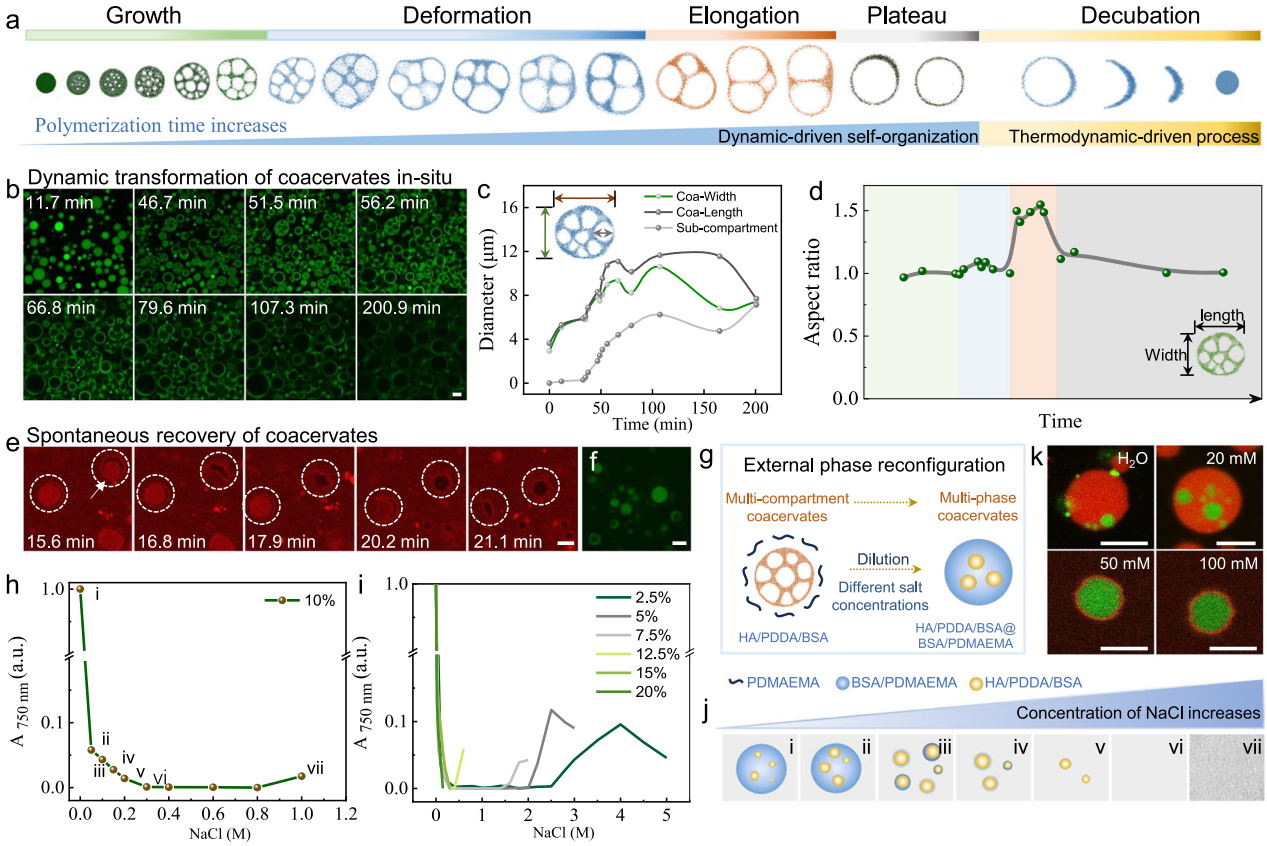

Fig. 3 | Dynamic structural evolution of coacervate droplets. a Schematic illustration of the structural evolution of coacervate droplets, showing approximately five periods including growth, deformation, elongation, plateau and decubation periods. **b** Time-dependent images of coacervates illuminated by 365 nm (20 W) for 3.5 h, showing that the coacervates transform into coacervate vesicles due to an increase in the concentration of PDMAEMA. **c** Plots of the length of multi-compartmental coacervates, width of multi-compartmental coacervates and diameter of sub-compartments. **d** Time-dependent aspect ratio of multi-compartmental coacervates. Aspect ratio = length of coacervate/width of coacervate. There are 19 data points reflecting the growth and fusion of internal sub-compartments. **e** Time-dependent CLSM images of coacervate vesicles, showing that vesicles spontaneously transform back into coacervates, (RBITC, red). **f** CLSM image of restored coacervates in (**e**) showing the sequestration of calcein. **g** Schematic illustration of external phase reconfigurations of coacervates. Generally, coacervate solution (HA/PDDA/BSA/DMAEMA) after polymerization under 405 nm for 6 h (10 μL) is mixed with NaCl solution of different concentrations (190 μL). **h** Typical turbidity of the coacervate polymerization solution after adding NaCl solution (10% w/v monomer content as a corresponding example shown in **j**). **i** Turbidity of the coacervate polymerization solution with different monomer contents. **j** Corresponding typical structural transformation of coacervates in (**h**). **k** NaCl-dependent CLSM images of reconstructed coacervates (15% w/v), (HA-AF, green), (Nile red, red). Scale bars, 5 μm. Source data are provided as a Source Data file.

coacervates could occur. We employed a confocal laser scanning microscope to observe the structural transformation of coacervates in-situ, and the polymerization was triggered under 365 nm ultraviolet irradiation (Fig. 3a). As shown in Fig. 3b and Supplementary Movie 1, the coacervates underwent a faster structural transformation within 3.5 h. A spherical coacervate was first transformed to multi-compartmental condensates, and the diameter of both the whole coacervate and the sub-compartment gradually increased. Then, with the increase in polymerization time, the coacervate matrix was further compressed, and the number of sub-compartments decreased. Subsequently, the inner sub-compartment fractured along with an immediate decrease in the diameter of the coacervate, ultimately forming spherical coacervate vesicles. These structural transformations exhibited an increase in length of coacervates, width of coacervates and diameter of sub-compartments (Fig. 3c), accompanied by fluctuations in aspect ratio (length of coacervates/width of coacervates ratio) (Fig. 3d). In general, the structural transition of coacervates with polymerization time was classified into four periods based on the aspect ratio, including growth, deformation, elongation and plateau period. The aspect ratio of coacervates at growth period was about 1, and the coacervates maintained an increase in diameter of whole coacervates and sub-compartments. Then, the aspect ratio of coacervates fluctuated around ~1.1 during deformation period, and this non-equilibrium state coacervates exhibited inner rupture of sub-compartments. Subsequently, the coacervates transformed into elongation period, during which the aspect ratio mutated to be ~1.5, and the coacervates converted to approximately two-chambers. Finally, the spherical coacervate vesicles were formed, and the aspect ratio rapidly decreased to be ~1 during plateau period.

To be of great interest, it is observed that the coacervate vesicles can spontaneously transform into spherical homogeneous coacervate droplets named decubation period. As shown in Fig. 3e, the RBITC initially was distributed in the sub-compartment, inner and outer membrane of coacervate vesicles (red fluorescence). The condensed phase flowed slowly to form thin and fragile sites as shown by the white arrows, and the vesicle ultimately broke at this point. During the adaptive process of the amorphous coacervate, the spherical homogeneous coacervate was spontaneously formed and reached a final thermodynamic equilibrium state. RBITC was distributed at the outer membrane of the final coacervates, which tracked the distribution of the polymers. The final coacervate matrix exhibited similar encapsulation behavior to the original HA/PDDA/BSA/DMAEMA coacervates (0 h) (Supplementary Figs. 26, 27).

Moreover, considering a large amount of PDMAEMA in bulk solution at the stage of high conversion rate of monomer, the solution became sticky. To further reveal the thermodynamic-driven structural transformation, we tried to implement the external phase reconfiguration of coacervates. The reaction solution was diluted with different concentrations of NaCl solution to drive the structural transformation of the multi-compartmental coacervates (Fig. 3g). Generally, the coacervate solution (HA/PDDA/BSA/DMAEMA) contained DMAEMA with different contents of 2.5%, 5%, 7.5%, 10%, 12.5%, 15% and 20% w/v, respectively, and was irradiated under 405 nm for 6 h. Then, 10 μL of reaction solution was mixed with 190 μL of NaCl solution and tested by UV-vis spectrum (Fig. 3h, i). The corresponding structural transformations in Fig. 3h were summarized in Fig. 3j. Typically, the external phase of reconstructed multiphase coacervates exhibited a lower critical salt concentration and was preferentially dissociated (i-ii). Then, the multiphase coacervate transformed into a condensed membrane-coated coacervate (iii-iv). When the critical salt concentration of the inner phase was reached, the coacervate dissociated completely (v-vi). At higher salt concentration, the precipitation occurred due to salting out of PDMAEMA (vii). Significantly, through the further investigation, the external phase of multiphase coacervate was composed of BSA and PDMAEMA, showing detention of Nile red, while its internal phase still maintained the composition of HA, PDDA and BSA, capable of taking in calcein (Fig. 3k, and Supplementary Figs. 28-30). The similar BSA/PDMAEMA composition was also observed in sub-compartments (Supplementary Figs. 31, 32).

The above exploration of external phase reconstruction further indicated that the coacervate vesicles tended to gradually break towards the formation of spherical homogeneous coacervate supported by a thermodynamic-driven process. We have demonstrated that the evolution process coupled with homeostasis of coacervates under the light stimulus, and the cycled evolution from homogeneous coacervate droplets into multi-compartmental coacervate, coacervate vesicle, and coacervate droplets are revealed, reminiscent of stress granules in living cells. When cells are subjected to stimuli such as high temperature, oxidative stress, and irradiation, the stress granules quickly form as temporary shelters for mRNA and proteins, and then dissociate after the disappearance of environmental stress. However, to be of our great surprise, the dynamic-driven formation of the transition state in this studied coacervate system could be fixed permanently by controlling the stimulation time 2-3 h under 405 nm, which then brings a special type of multi-compartmental structure in the coacervate droplet community with spatial regulation of biological reaction.

Stability of multi-compartmental coacervates

It is found that the formed multi-compartmental coacervates could maintain the morphology well over several months (Supplementary Fig. 33). Despite being subjected to the mechanical stirring at 100 rpm for 4 h (Supplementary Fig. 34e–g), there was no emergence of coalescence or dissociation of multi-compartments. As a control experiment, HA/PDDA coacervates and HA/PDDA/BSA/DMAEMA coacervates (0 h) were condensed at the bottom or nearly completely dissociated (Supplementary Fig. 35). By contrast, the multi-compartmental coacervates could well resist centrifugation force at $300 \times g$ for 1 min. Even after undergoing five cycles of centrifugal treatment, the resuspended multi-compartmental coacervates still maintained the intact structure of over 80% with almost invariable diameter, indicating robustness and stability of the formed multi-compartmental coacervates (Fig. 4a and Supplementary Figs. 36, 37). Even if the centrifugal force was increased at $2600 \times g$ for 3 min, no homogeneous coacervates or large-sized coacervates were formed. The results showed restricted phase separation in the interior of multi-compartments, and the reconfigured coacervate still showed regional partition for calcein and rhodamine B (Fig. 4b). In addition, the multi-compartmental coacervates can be formed in a wide pH range from 4 to 10 (Supplementary Fig. 38).

We speculated that the formation of PDMAEMA reduced the drop adhesion force (DAF) between the coacervate droplets, which was one of the key factors for the long-term structural stability of multi-compartments. We detected the interaction force between the coacervates and the corresponding substrate surface prepared by depositing the same coacervate solution onto a glass slide. At the contact interface between the droplet and the surface, there are three forces: Fγ, interfacial tension; Fp, caused by interface capillary pressure difference ΔP; Fa, surface-applied force for droplets, representing mutual compression or attraction between the droplet and the surface. The direction and magnitude of Fa depend on the values of Fγ and Fp to maintain equilibrium of forces at the contact interface (Fγ + Fp + Fa = 0). By tracking the process of the coacervate droplet breaking on the surface, the contact angle (θ) and the interaction force (DAF) between the droplet and the surface were directly calculated based on the contour as shown in Fig. 4c and Supplementary Fig. 39. As shown in Fig. 4d, the drop adhesion force (DAF)/contact angle (θ) between the HA/PDDA/BSA coacervate droplet and the HA/PDDA/BSA substrate or the multi-compartmental coacervate droplet and the multi-compartmental coacervate substrate were tested. The process was mainly described as three stages: a to b represented that the droplet began to contact the surface, and both DAF and θ rapidly increased; b to c exhibited that moving the substrate towards the opposite direction induced the elongation and deformation of the droplet; c to d implied the breakup of the droplet. DAF between HA/PDDA/BSA coacervate droplet and HA/PDDA/BSA substrate was estimated to be 51.85 ± 3.64 μN, and that between the multi-compartmental coacervate droplet and its substrate was estimated to be 30.14 ± 6.4 μN, indicating a lower DAF between the multi-compartmental coacervates. This was also supported by the investigation of contact angles. After the droplet breakup at position d, the contact angle of HA/PDDA/BSA coacervate droplet with its substrate was 75.61^0, while that of the multi-compartmental coacervate droplet with its substrate was 104.17^0 ($> 90^0$), which revealed that multi-compartmental coacervates tended to repel each other. These were also consistent with directly characterizing the contact angle of both HA/PDDA/BSA coacervate droplet with its substrate, as well as the multi-compartmental coacervate droplet with its substrate, and the contact angle was detected to be 57.4^0 and 102.1^0, respectively (Fig. 4e).

Meanwhile, the zeta potential of the multi-compartmental coacervates was determined to be approximately 59.7 mV. Compared with the zeta potential of −10.28 ± 1.5 mV of DMAEMA, that of PDMAEMA converted to a positive value of 13.4 ± 2.8 mV (Fig. 4f), which then contribute to the other key factor in maintaining structural stability of multi-compartmental coacervates. To further understand the details of electrostatic interaction, the electrostatic potential (ESP) mapped van der Waals surface of DMAEMA and PDMAEMA was demonstrated by DFT simulation calculation[47–49]. The ESP minima/maxima points were quantitatively analyzed and labeled on the surface. The ESP minimum of DMAEMA was calculated to be -43.13 kcal/mol, and a larger ESP maximum near the carbon-carbon double bonds was observed (19.38 kcal/mol) (Fig. 4g). In contrast, PDMAEMA exhibited multiple larger ESP maxima, and showed negative ESP minimum near nitrogen atoms (Fig. 4h, i), which contributes to the possibility of PDMAEMA as a Lewis base. As a result, PDMAEMA, with its positive zeta potential, interacted with negatively charged BSA in H_2O to maintain the stability of multi-compartmental coacervates.

Based on the above observations, we proposed the formation process of multi-compartmental coacervates as follows. Along with polymerization proceeding, PDMAEMA is preferentially generated in the interior of coacervates due to high BSA partition, which increases the electrostatic interaction to induce the formation of inner vacuoles of coacervates. With further increases in concentration of PDMAEMA,

https://doi.org/10.1038/s41467-025-57069-1

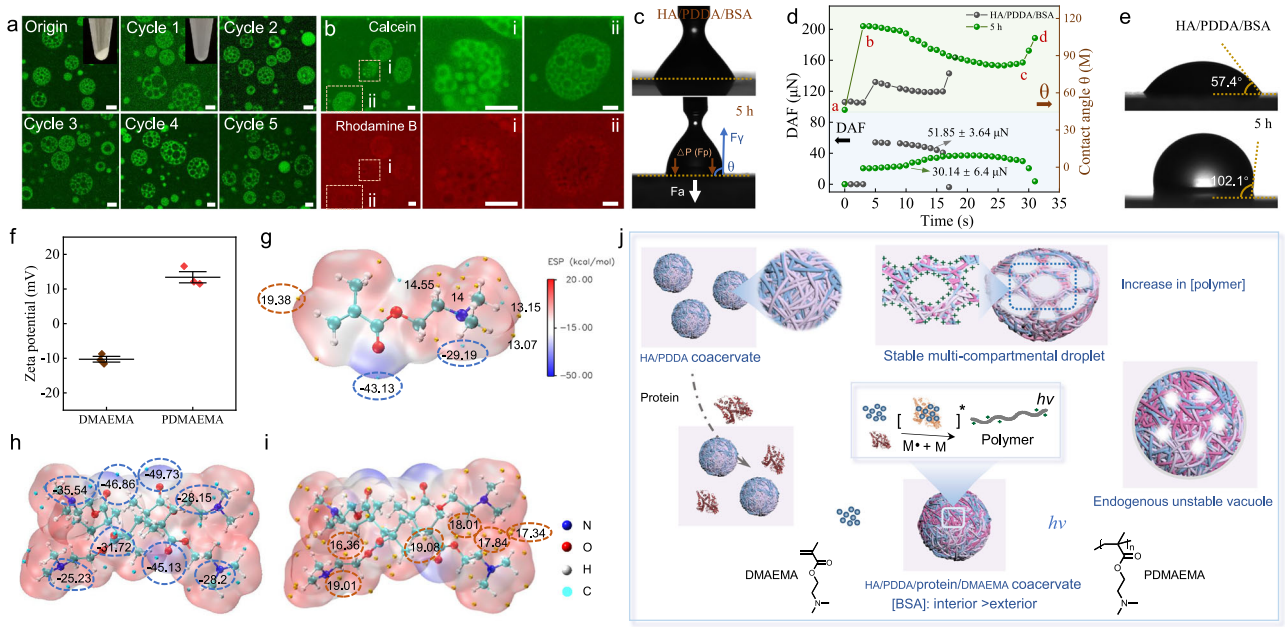

Fig. 4 | Long-term stability of multi-compartmental coacervates. a CLSM images of multi-compartmental coacervates undergoing five cycles of centrifugation at 300 × *g* for 1 min. The insets are photographs of centrifugation and redispersion of multi-compartmental coacervates. **b** CLSM images of restricted phase reconfiguration inside multi-compartmental coacervates by centrifugation at 2600 × *g* for 3 min, showing regional sequestration of coacervates for calcein and rhodamine B. The multi-compartmental coacervates in (**a**, **b**) are obtained by 405 nm illumination for 2.5 h. **c** Contour images of the HA/PDDA/BSA droplet or the multi-compartmental coacervate droplet (5 h) contacting the corresponding substrate, showing that the droplet will fracture from the substrate. **d** Drop adhesion force (DAF)/contact angle (θ) between HA/PDDA/BSA droplets or multi-compartmental coacervate droplets with the corresponding substrate, obtained by calculating the contour of the droplet contacting the surface and then breaking from the surface. **e** Contact angle between HA/PDDA/BSA droplets or multi-compartmental coacervate droplets onto the corresponding substrate surface. The multi-compartmental coacervates in (c-e) are obtained by 405 nm illumination for 5 h. The substrate was prepared by depositing the same solution onto a glass slide and drying naturally. **f** Zeta potential of DMAEMA and PDMAEMA in H_2O at 25 °C. Data are presented as mean ± s.d. ($n = 3$). **g** Electrostatic potential (ESP) mapped van der Waals surface of DMAEMA. Electrostatic potential mapped van der Waals surface of PDMAEMA with ESP minima (**h**) and maxima distribution (**i**). The cyan/orange points represent ESP minima/maxima, respectively. Blue and orange dashed boxes represent the large minima and maxima, respectively. **j** Proposed formation process of stable multi-compartmental coacervates. Scale bars, 5 μm. Source data are provided as a Source Data file.

the positively charged PDMAEMA stabilizes at interfaces/surfaces against the disappearance and coalescence of internal vacuoles. At the same time, a decrease in osmotic pressure of bulk solution also promotes the generation of sub-compartments, and osmotic pressure balance between the internal sub-compartment and the external bulk solution is an important factor to keep multi-compartmental coacervates stable (Fig. 4j).

Moreover, given the good stability of the formed multi-compartments, the developed phase separation method would be a robust technique for creating various coacervate-based functionalized ensembles. In this regard, we employed various intracellular proteins-mediated photopolymerization to investigate the structural transformation of coacervates, including ribonuclease A (RNase A) and lysozyme (Fig. 5a and Supplementary Fig. 40). As a result, these proteins-mediated photopolymerization also induced coacervate droplets to transform into multi-compartments, showing similar compartmental sequestration characteristics for calcein (green) and RBITC. Furthermore, we also tried to incorporate *E. coli* into PDDA prior to addition of HA to give rise to bacteria-enriched coacervate droplets, followed by the addition of BSA and DMAEMA (Fig. 5b). Under 405 nm LED light for 2.5 h, a type of coacervates/bacteria ensemble was formed with good structural stability over 1 week (Fig. 5d, e and Supplementary Fig. 41). By contrast, the coacervates/bacteria assemblies formed under dark condition, showed irreversible coalescence of the coacervates/bacteria assemblies (Fig. 5c).

Transition and regulation of interfacial/homogeneous catalysis

The phase separation is of great significance for regulating the spatial location of enzymes to affect certain biological reactions. We explored the spatial location of RBITC-modified lipase. The lipase-RBITC can be specially distributed into sub-compartments of the multi-compartmental coacervates, while its catalytic substrate, 4-methylumbelliferone butyrate, and the blue fluorescent product, 4-methylumbelliferone, were both retained in the coacervate matrix (Fig. 5f). The size of multi-compartmental coacervates could be regulated by controlling the polymerization time (Supplementary Fig. 34). Accordingly, the catalytic efficiency of lipases would be varied. We selected the multi-compartmental coacervate with sub-compartments of different sizes, obtained by polymerization under 405 nm for 1.5 h, 2.5 h and 3.5 h, respectively. The interfacial catalysis of lipases was successfully monitored as shown in Fig. 5g and Supplementary Fig.42a, b. After 400 s of reaction, the fluorescent intensity of the product based on multi-compartmental coacervates of 1.5 h photopolymerization showed the highest catalytic rate. With the size of sub-compartment increasing, the interfacial catalytic efficiency decreased accordingly. The catalytic efficiency of lipases based on multi-compartmental coacervates of 1.5 h, 2.5 h and 3.5 h, increased by approximately 29.4, 11.5 and 8.7 times compared with that in the absence of coacervates, respectively. (Fig. 5h and Supplementary Fig. 42c).

Especially, it is worth noting that after 300 days, the multi-compartmental coacervates could still keep the morphology, and maintain their sequestration characteristic of separating different substances into distinct regions to achieve the efficient organization and coordination of spatial biochemical reactions. Notably, the multi-compartmental coacervates after 300 days can encapsulate RBITC into coacervate matrix (Supplementary Fig. 43). In this case, by adding

https://doi.org/10.1038/s41467-025-57069-1

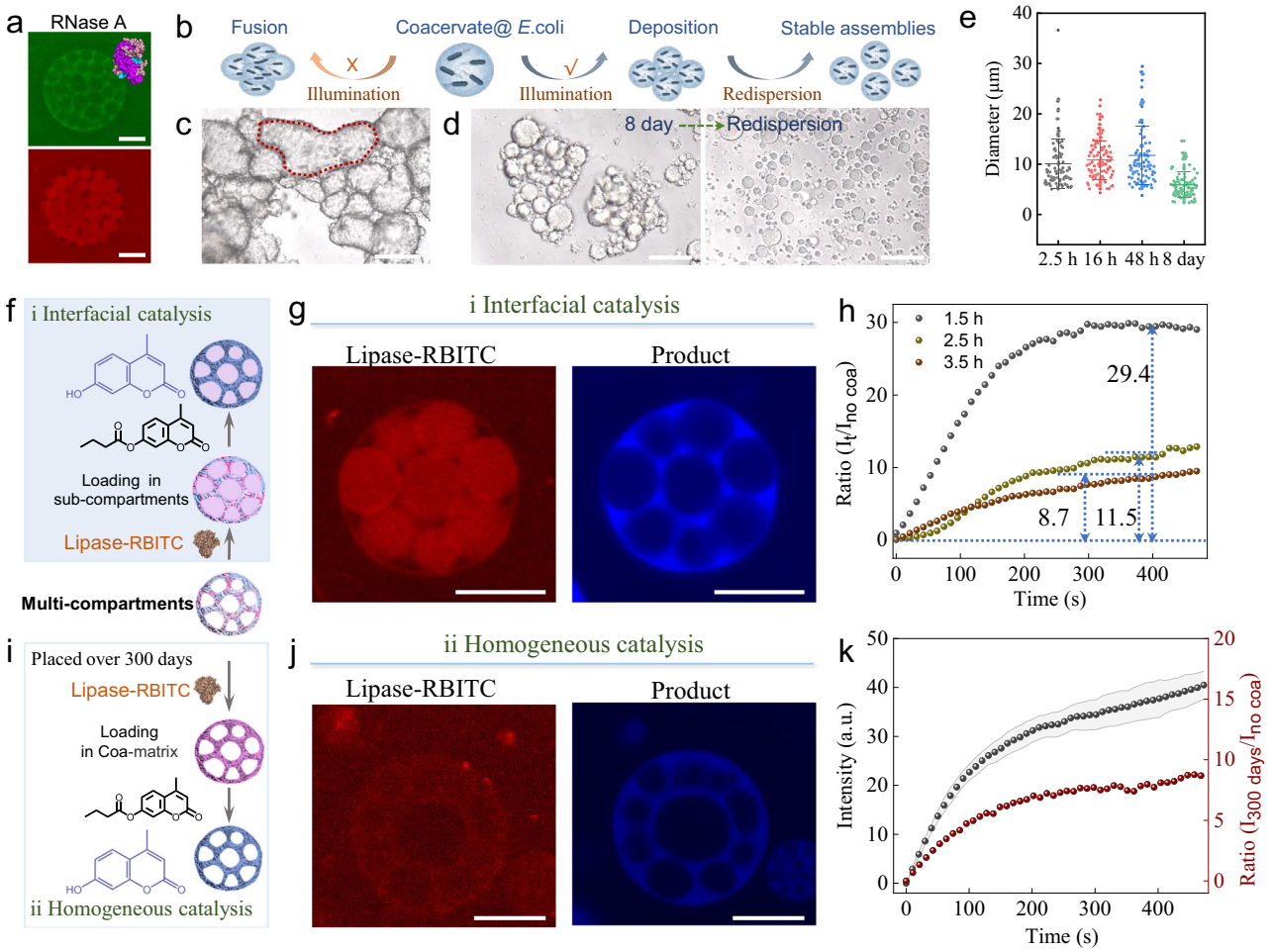

Fig. 5 | Construction of various coacervate assemblies and time-dependent transition of interfacial/homogeneous catalysis. a CLSM images of HA/PDDA/RNase A/DMAEMA multi-compartmental coacervates induced by RNase A-mediated photopolymerization under 405 nm for 2.5 h, showing compartmental sequestration for calcein (green) and RBITC (red). **b** Schematic illustration of the stable coacervates/bacteria assemblies formation. **c** Microscopy image of coacervates/bacteria assemblies without polymerization observed after 24 h, showing the fusion between the coacervates/bacteria assemblies. **d** Microscopy images of coacervates/bacteria assemblies formed under 405 nm illumination for 2.5 h, observed on the eighth day, showing the assemblies naturally deposited and gathered at the bottom, but were still re-dispersed (2.5% w/v monomer content). **e** Diameter statistics of coacervates/bacteria assemblies. Scale bars in (**c**, **d**), 50 μm. Data are presented as mean ± s.d. ($n = 94$). **f** Schematic illustration of lipase-RBITC-mediated interfacial catalysis. **g** CLSM images of lipase-RBITC-mediated interfacial catalysis in multi-compartmental coacervates obtained by photopolymerization under 405 nm for 3.5 h. Lipase-RBITC was distributed in sub-compartments (red fluorescence), while the catalytic product 4-methylumbelliferone (blue fluorescence) was distributed in the coacervate matrix after 400 s of catalytic reaction. **h** The fluorescent ratio statistics of the catalytic product in multi-compartmental coacervates of different sizes or no coacervates. The multi-compartmental coacervates of different sizes were obtained by photopolymerization under 405 nm for 1.5 h, 2.5 h and 3.5 h, respectively. **i** Schematic illustration of lipase-RBITC-mediated homogeneous catalysis after 300 days. **j** CLSM images of homogeneous catalysis of lipase-RBITC in the multi-compartmental coacervates, formed by 405 nm illumination for 2.5 h and applied after 300 days, showing that lipase-RBITC (red) and the catalytic product (blue) were both distributed in the coacervate matrix after 400 s of catalytic reaction. **k** Corresponding fluorescent intensity and ratio statistics of the catalytic product generated by lipase-RBITC-mediated homogeneous catalysis in 300 days multi-compartmental coacervates. The shaded region represents the error interval of standard deviation of the mean points. Scale bars in (**g**, **j**), 5 μm. Source data are provided as a Source Data file.

lipase-RBITC into the multi-compartmental coacervates, we examined homogeneous catalysis of lipase-RBITC in the multi-compartments applied after 300 days (Fig. 5i). The homogeneous catalysis of lipase-RBITC was successfully carried out along with the generation of a blue fluorescent product, and the fluorescence intensity of catalytic product was enhanced about 8 times compared with that in the absence of coacervates (Fig. 5j, k), which was slightly lower than the catalytic rate of homogeneous catalysis of lipase-FITC in multi-compartments coacervate obtained by 3.5 h polymerization (Supplementary Fig. 44).

Our study reveals the endogenous self-organization process of coacervates induced by protein-mediated polymerization under light stimulation. By exploring the dynamic structural evolution of coacervates, we found that the mechanism of coacervate phase transition is not permanent, but evolves with the environment. We conclude that the dynamic transformation of coacervates involves both assembly and disassembly: the accumulation of products during chemical reaction process will result in morphological deformation, relying on the dynamic control to drive complex structural transformation and the thermodynamic control to reach phase equilibrium, and the behavior of phase separation is related to multiple factors, such as external irradiation, metabolites, enzyme catalytic processes, etc. By controlling the duration of light stimulation, the dynamic transformation of coacervates facilitates the formation of stable multi-compartmental coacervates, which exhibits the spatial separated encapsulation of dyes/proteins, and enhances interfacial catalytic efficiency by regulating location of enzymes. Our studies reveal that combining osmotic pressure and electrostatic interaction could induce the production of sub-compartments and stabilize

multi-compartments. High zeta potential at the interface between the matrix and the sub-compartments/bulk phase overcomes limitation of structural stability. Even after 300 days, the multi-compartmental coacervates still show the spatial sequestration characteristics. Based on the distribution of lipase in coacervate-matrix after 300 days, homogeneous catalysis of lipases is efficiently achieved. Therefore, it is anticipated that these studies could provide an available approach in design of long-term stable multi-compartmental microreactor models or hierarchical assemblages combined with the natural versatility of modules. Many studies have revealed the importance of protein domains in phase separation. By our researching, we realize that the functionality of proteins also plays a crucial role, especially in complex phase separation dynamic processes. We hope to promote understanding the phase separation mechanism to help effectively design and apply phase separation to regulate cellular physiological process.

Methods

Characterization methods

Optical images were performed on a Leica DMi8 manual inverted fluorescence microscope at 40× magnifications. Image J software was employed to measure the diameters of the coacervates. Confocal fluorescence images were performed on a Leica SP8 Laser scanning confocal microscope. Scanning electron microscopy (SEM) image of dried samples was obtained with a SU8000 instrument. ^{1}H NMR spectra of monomer/polymer solutions were measured on a Bruker Avance-400 MHz NMR spectrometer using D_2O as the solvent and DMF as the reference. The test result was analyzed using MestReNova. UV-vis spectrum measurements were measured on a PerkinElmer spectrophotometer (Lambda 750S, USA). Zeta potential measurements were performed using Malvern Zetasizer Nano-ZSP at 25 °C. Agarose gel electrophoresis was conducted at 100 V using TAE buffer as running buffer. The samples were loaded by mixing 4 μL of sample, 1 μL of 6× loading buffer, with 1 μL of SYBR Green I. Drop adhesion force (DAF)/contact angle (θ) were performed on an Optical Surface Analyzer (OSA 100S-M, NBSI). Density functional theory (DFT) calculations were performed by Gaussian 09 software with DFT-D3 (BJ) corrected B3LYP functional (B3LYP-D3 (BJ)). Geometry optimizations were carried out at B3LYP-D3 (BJ)/6-311 G (d, p) level coupled with IEFPCM solvent model (water).

Dynamic transformation of coacervates induced by protein-mediated photopolymerization

HA (3 mL, 15 mg/mL) and PDDA (1 mL, 85 mg/mL) were mixed to prepare the coacervate solution. Take 1 mL of coacervate solution, and then add BSA (1 mL, 15 mg/mL) and DMAEMA (0.1 mL) sequentially to obtain reaction mixture in a glass vial. Next, the vial was sealed and purged with Argon for 30 min. After anaerobic treatment, the vial was irradiated under violet LED light (405 nm, 20 W) at room temperature. Aliquots were taken at predetermined time intervals, and then centrifuged at 5300 × *g* for 10 min. The supernatant and precipitation were diluted with D_2O of 600 mM NaCl for ^{1}H NMR spectrum.

Fluorescence recovery after photobleaching (FRAP)

FRAP experiment is used to describe the mobility of coacervates. The multi-compartmental coacervates were firstly prepared. Generally, HA (0.45 mL, 15 mg/mL) and PDDA (0.15 mL, 85 mg/mL) were mixed to prepare the HA/PDDA coacervate solution. Take 0.5 mL of coacervate solution, and then add BSA (0.5 mL, 15 mg/mL), DMAEMA (0.05 mL) and HA-AF (30 μL, 10 mg/mL, green fluorescence) sequentially to obtain reaction mixture in a glass vial. The vial was sealed and purged with Argon for 30 min. After anaerobic treatment, the vial was irradiated under violet LED light (405 nm, 20 W) at room temperature for 2.5 h to obtain the multi-compartmental coacervates. Then, FRAP experiment was performed on a laser scanning confocal microscope. The different positions of the multi-compartmental coacervate were selected as a region of interest (ROI), and then ROI was bleached with 488 nm laser with 100% energy intensity, and time-lapse movies were recorded for fluorescent intensity analysis.

Structural transformation of coacervates in-situ

The coacervate was firstly prepared according to the above procedure. HA (0.45 mL, 15 mg/mL) and PDDA (0.15 mL, 85 mg/mL) were mixed to prepare the HA/PDDA coacervate solution. Take 0.5 mL of coacervate solution, and then add BSA (0.5 mL, 15 mg/mL), DMAEMA (0.05 mL) and HA-AF (30 μL, 10 mg/mL) sequentially to obtain reaction mixture in a glass bottom dish. The dish was sealed and purged with Argon for 30 min. After that, the dish was placed under laser scanning confocal microscope with 488 nm laser, and irradiated under violet LED light (365 nm, 20 W) at room temperature. Time-lapse movies were recorded for fluorescent intensity analysis. The length of the coacervates, width of the coacervates and diameter of the sub-compartments were measured by Image J software.

External phase reconfigurations of coacervates

Generally, HA (0.45 mL, 15 mg/mL) and PDDA (0.15 mL, 85 mg/mL) were mixed to prepare the HA/PDDA coacervate solution. Take 0.5 mL of coacervate solution, and then add BSA (0.5 mL, 15 mg/mL), HA-AF (30 μL, 10 mg/mL) and DMAEMA with different content of 2.5%, 5%, 7.5%, 10%, 12.5%, 15% and 20% w/v, respectively. The mixture was sealed and purged with Argon for 30 min. The reaction was carried out under 405 nm illumination for 6 h. After that, take 10 μL of reaction solution, followed by mixing 190 μL of NaCl solution of different concentrations, and then observe under a laser scanning confocal microscope.

Stability of multi-compartmental coacervates

The stability of multi-compartmental coacervate was investigated by centrifugation at different rates. The multi-compartmental coacervates were obtained by polymerization under 405 nm illumination for 2.5 h according to the above method. Then, 1 mL of multi-compartmental coacervates underwent five cycles of centrifugation at 300 × *g* for 1 min. After each cycle, 20 μL of coacervate was mixed with 1 μL of dyes, and then observed under a laser scanning confocal microscope. For inner phase reconfiguration of multi-compartmental coacervates, the same procedure was implemented except for increasing the centrifugal rate to 2600 × *g* for 3 min.

Drop adhesion force (DAF) measurement

DAF was used to assess the interaction between coacervates performed on an Optical Surface Analyzer (OSA 100S-M, NBSI). Generally, the substrate was first prepared by depositing the corresponding coacervate solution onto a glass slide and dried naturally at room temperature. The corresponding coacervate solution was inhaled into a syringe pump (1 mL). The general process was as follows: the droplet was produced through compression, hanging at the tip of the needle, and moving the substrate began to contact with the droplet. Then, moving the substrate towards the opposite direction induced the droplet elongation and deformation until the droplet breakup. By tracking the process of the coacervate droplet breaking on the surface, the contact angle (θ) and DAF between the droplets and the corresponding surface can be directly calculated by the contour as shown in Supplementary Fig. 39.

Homogeneous/interfacial catalysis in multi-compartmental coacervates

30 μL of multi-compartmental coacervates formed by the different polymerization time was mixed with lipase-FITC (15 μL, 10 mg/mL) or lipase-RBITC (15 μL, 10 mg/mL), while lipase-FITC and lipase-RBITC were encapsulated in matrix and sub-compartments, respectively. Take 5 μL of multi-compartmental coacervates with lipase-FITC or lipase-RBITC onto a glass bottom dish, and then add 2 μL of

4-methylumbelliferone butyrate in-situ (4.19 mg/mL). The catalytic reaction was monitored by a laser scanning confocal microscope. As a control, the equal volume of PBS (pH 8.0, 50 mM) instead of multi-compartmental coacervates or lipase was added into the reaction system, followed by the addition of 4-methylumbelliferone butyrate, showing no fluorescence or low fluorescence intensity.

HA labeled by fluorescence dyes

HA was labeled by 5-Aminofluorescein utilizing the reaction between carboxyl and amino groups. 100 mg of HA was dissolved in 2 mL of PBS buffer solution (50 mM, pH = 6.5), and then added 3 mL of 5-aminofluorescein solution (2.3 mg/mL in DMSO). The reaction was initiated by adding N-(3-dimethylaminopropyl)-N′-ethylcarbodiimide hydrochloride (EDAC, 11 mg) solution and stirred at 200 rpm at room temperature for 12 hours. After that, the solution was dialyzed (dialysis tube ~35 kDa MWCO) extensively against Milli-Q water and purified by using a filter (0.45 μm). After freeze-drying, the green fluorescent HA-AF was obtained.

BSA/Lipase labeled by fluorescence dyes

BSA/Lipase (50 mg) was dissolved in 2.0 mL of PBS buffer solution (50 mM, pH = 8), and then FITC (50 μL, 1 mg/mL in DMSO) or RBITC (50 μL, 1 mg/mL in H_2O) was added dropwise. The mixture was stirred at 200 rpm at room temperature for 6 hours. After that, the solution was dialyzed (dialysis tube ~3 kDa MWCO) extensively against Milli-Q water to remove unreacted dyes. After freeze-drying, the fluorescent protein BSA-FITC, lipase-FITC and lipase-RBITC were obtained.

Synthesis of fluorescent PMAEB

Ethyl bromide salt of dimethylaminoethyl methacrylate (MAEB) was firstly synthesized. Generally, methacrylic acid 2-(dimethylamino) ethyl ester (DMAEMA) and bromoethane were mixed at molar ratio: 1:1 into 2 mL of acetone with 0.2% (molar ratio) hydroquinone monomethyl ether (as an inhibitor). Then, the reaction was carried out at 40 °C for 24 h under a reflux condenser. The product was purified by precipitation in cold diethyl ether for two times to obtain MAEB. Next, the red fluorescent PMAEB was prepared by a traditional thermo-initiated polymerization process. Generally, MAEB (200 mg, 0.752 mmol), AIBN (0.33 mg, 0.002 mmol) and HEMA (3 mg, 0.023 mmol) were added into 2 mL of DMF in a 5 mL round bottom flask. After that, the flask was sealed with parafilm and purged with Argon for 30 min. The reaction was carried out at 65 °C for 6 h and then purified by diethyl ether/petroleum ether (1:2 volume ratio) to obtained pure PMAEB. After that, the red fluorescent PMAEB was prepare by mixing PMAEB (50 mg), RBITC (100 μL, 1 mg/mL in H_2O) in 2.0 mL of PBS buffer solution (50 mM, pH = 8). The mixture was stirred at 200 rpm at room temperature for 8 hours. After that, the solution was dialyzed (dialysis tube ~3 kDa MWCO) extensively against Milli-Q water to remove unreacted dyes. After freeze-drying, the red fluorescent PMAEB-RBITC was obtained.

Synthesis of fluorescent PDMAEMA

Generally, DMAEMA (400 mg, 2.54 mmol), AIBN (0.33 mg, 0.002 mmol) and fluorescein O-methacrylate (FMA, 2 mg, 5 μmol) were added into 2 mL of acetonitrile in a 5 mL round bottom flask. After that, the flask was sealed with parafilm and purged with Argon for 30 min, and then the reaction was carried out at 65 °C for 6 h. The mixture was purified in diethyl ether/petroleum ether for three times to remove unreacted monomer, and then dried at room temperature under vacuum for 24 h. The green fluorescent PDMAEMA-FMA was obtained.

Contact angle measurement

The substrate was firstly prepared by depositing the corresponding coacervate solution onto a glass slide and dried naturally at room temperature. Then, the corresponding coacervate was dropped onto the substrate surface, and the contact angle was measured.

Coacervates/bacteria assemblies construction

Generally, overnight cultured *E*. coli was washed three times with water by centrifugation (2124 × *g*, 3 min) and resuspended in deionized water. Mix *E*. coli into PDDA prior to addition of HA to obtain bacteria-enriched coacervate droplets, followed by addition of BSA (7.5 mg/mL) and DMAEMA (2.5% w/v). After Argon deoxygenation for 20 min, the polymerization of coacervates/bacteria assemblies was implemented under 405 nm illumination for 2.5 h, and then sustained to observe under microscopy at 16 h, 48 h and 8 days. By contrast, the coacervates/bacteria assemblies were placed without illumination for 24 h, showing fusion between the coacervates/bacteria assemblies.

Fluorescent dyes encapsulation

Generally, 1 μL of fluorescent dyes (0.1 mg/mL) was added into 20 μL coacervates or multi-compartmental coacervates solution. After that, taking 5 μL of mixing solution was observed by a laser scanning confocal microscope. The coacervate was randomly selected for fluorescence intensity analysis.

General procedure of coacervate polymerization in different pH solutions

HA (3 mL, 15 mg/mL) and PDDA (1 mL, 85 mg/mL) were mixed to prepare the coacervate solution. Take 1 mL of coacervate solution, and then add 1 mL of BSA solution (15 mg/mL) with different pH (PBS buffer, 20 mM, pH = 4, 7, 10) and DMAEMA (0.1 mL) sequentially to obtain reaction mixture in a glass vial. Next, the vial was sealed and purged with Argon for 20 min. After anaerobic treatment, the vial was irradiated under violet LED light (405 nm, 20 W) at room temperature. After 2.5 h, the samples were observed by a laser scanning confocal microscope.

Structural transformation of coacervates induced by RNase A/lysozyme -mediated photopolymerization

HA (3 mL, 15 mg/mL) and PDDA (1 mL, 85 mg/mL) were mixed to prepare the coacervate solution. Take 1 mL of coacervate solution, and then add 1 mL of RNase-A (15 mg/mL) or lysozyme (3.75 mg/mL) and DMAEMA (0.1 mL) sequentially to obtain reaction mixture in a glass vial. Next, the vial was sealed and purged with Argon for 30 min. After anaerobic treatment, the vial was irradiated under violet LED light (405 nm, 20 W) at room temperature. Aliquots were taken at predetermined time intervals, and then centrifuged at 5300 × *g* for 10 min. The supernatant and precipitation were diluted with D_2O of 600 mM NaCl for ^1H NMR spectrum.

Reporting summary

Further information on research design is available in the Nature Portfolio Reporting Summary linked to this article.

Data availability

All experimental data supporting the findings of the study are available within the article and its Supplementary Information. Source data are provided with this paper.

References

1. Allen, M. E. et al. Biomimetic behaviors in hydrogel artificial cells through embedded organelles. *Proc. Natl Acad. Sci. USA* **120**, e2307772120 (2023).
2. Bayoumi, M., Bayley, H., Maglia, G. & Sapra, K. T. Multi-compartment encapsulation of communicating droplets and droplet networks in hydrogel as a model for artificial cells. *Sci. Rep. -UK*. **7**, 45167 (2017).

3. Galanti, A. et al. A floating mold technique for the programmed assembly of protocells into protocellular materials capable of non-equilibrium biochemical sensing. *Adv. Mater.* **33**, 2100340 (2021).
4. Stano, P. Is research on "Synthetic Cells" moving to the next level? *Life* **9**, 3 (2018).
5. Abbas, M., Lipiński, W. P., Wang, J. & Spruijt, E. Peptide-based coacervates as biomimetic protocells. *Chem. Soc. Rev.* **50**, 3690–3705 (2021).
6. Cakmak, F. P., Choi, S., Meyer, M. O., Bevilacqua, P. C. & Keating, C. D. Prebiotically-relevant low polyion multivalency can improve functionality of membraneless compartments. *Nat. Commun.* **11**, 5949 (2020).
7. Deshpande, S. et al. Spatiotemporal control of coacervate formation within liposomes. *Nat. Commun.* **10**, 1800 (2019).
8. Lu, T. et al. Endocytosis of coacervates into liposomes. *J. Am. Chem. Soc.* **144**, 13451–13455 (2022).
9. Mu, W. et al. Superstructural ordering in self-sorting coacervate-based protocell networks. *Nat. Chem.* **16**, 158–167 (2024).
10. Zhou, P. et al. Engineered artificial membraneless organelles in saccharomyces cerevisiae to enhance chemical production. *Angew. Chem. Int. Ed.* **62**, e202215778 (2023).
11. Iglesias-Artola, J. M. et al. Charge-density reduction promotes ribozyme activity in RNA-peptide coacervates via RNA fluidization and magnesium partitioning. *Nat. Chem.* **14**, 407–416 (2022).
12. Drobot, B. et al. Compartmentalised RNA catalysis in membrane-free coacervate protocells. *Nat. Commun.* **9**, 3643 (2018).
13. Jobdeedamrong, A. et al. Assembly of biomimetic microreactors using caged-coacervate droplets. *Nanoscale* **15**, 2561–2566 (2023).
14. Cao, S. et al. Dipeptide coacervates as artificial membraneless organelles for bioorthogonal catalysis. *Nat. Commun.* **15**, 39 (2024).
15. Xu, C., Martin, N., Li, M. & Mann, S. Living material assembly of bacteriogenic protocells. *Nature* **609**, 1029–1037 (2022).
16. Altenburg, W. J. et al. Programmed spatial organization of biomacromolecules into discrete, coacervate-based protocells. *Nat. Commun.* **11**, 6282 (2020).
17. Gao, N. & Mann, S. Membranized coacervate microdroplets: from versatile protocell models to cytomimetic materials. *Acc. Chem. Res.* **56**, 297–307 (2023).
18. Ji, Y., Lin, Y. & Qiao, Y. Plant cell-inspired membranization of coacervate protocells with a structured polysaccharide layer. *J. Am. Chem. Soc.* **145**, 12576–12585 (2023).
19. Li, J., Liu, X., Abdelmohsen, L., Williams, D. S. & Huang, X. Spatial organization in proteinaceous membrane-stabilized coacervate protocells. *Small* **15**, 1902893 (2019).
20. Liu, S. et al. Enzyme-mediated nitric oxide production in vasoactive erythrocyte membrane-enclosed coacervate protocells. *Nat. Chem.* **12**, 1165–1173 (2020).
21. Mason, A. F., Buddingh, B. C., Williams, D. S. & van Hest, J. C. M. Hierarchical self-assembly of a copolymer-stabilized coacervate protocell. *J. Am. Chem. Soc.* **139**, 17309–17312 (2017).
22. Zhao, C. et al. Membranization of coacervates into artificial phagocytes with predation toward bacteria. *ACS Nano* **15**, 10048–10057 (2021).
23. Kubota, R., Torigoe, S. & Hamachi, I. Temporal stimulus patterns drive differentiation of a synthetic dipeptide-based coacervate. *J. Am. Chem. Soc.* **144**, 15155–15164 (2022).
24. Donau, C., Späth, F., Stasi, M., Bergmann, A. M. & Boekhoven, J. Phase transitions in chemically fueled, multiphase complex coacervate droplets. *Angew. Chem. Int. Ed.* **134**, e202211905 (2022).
25. Zubaite, G., Hindley, J. W., Ces, O. & Elani, Y. Dynamic reconfiguration of subcompartment architectures in artificial cells. *ACS Nano* **16**, 9389–9400 (2022).
26. Capasso, P. U. et al. Programmable zwitterionic droplets as biomolecular sorters and model of membraneless organelles. *Adv. Mater.* **34**, 2104837 (2022).
27. Mountain, G. A. & Keating, C. D. Formation of multiphase complex coacervates and partitioning of biomolecules within them. *Biomacromolecules* **21**, 630–640 (2020).
28. Lu, T. & Spruijt, E. Multiphase complex coacervate droplets. *J. Am. Chem. Soc.* **142**, 2905–2914 (2020).
29. Pederson, T. The nucleolus. *Cold Spring Harb. Perspect. Biol.* **3**, a000638 (2011).
30. Gall, J. G. The centennial of the Cajal body. *Nat. Rev. Mol. Cell Bio.* **4**, 975–980 (2003).
31. Protter, D. & Parker, R. Principles and properties of stress granules. *Trends Cell Biol.* **26**, 668–679 (2016).
32. Shan, Z. et al. Basal condensation of Numb and Pon complex via phase transition during drosophila neuroblast asymmetric division. *Nat. Commun.* **9**, 737 (2018).
33. Sun, D., Wu, R., Zheng, J., Li, P. & Yu, L. Polyubiquitin chain-induced p62 phase separation drives autophagic cargo segregation. *Cell Res* **28**, 405–415 (2018).
34. Du, M. & Chen, Z. J. DNA-induced liquid phase condensation of cGAS activates innate immune signaling. *Science* **361**, 704–709 (2018).
35. Zhou, Z., Maxeiner, K., Ng, D. Y. & Weil, T. Polymer chemistry in living cells. *Acc. Chem. Res.* **55**, 2998–3009 (2022).
36. Wolozin, B. & Ivanov, P. Stress granules and neurodegeneration. *Nat. Rev. Neurosci.* **20**, 649–666 (2019).
37. Cui, Q. et al. Diverse CMT2 neuropathies are linked to aberrant G3BP interactions in stress granules. *Cell* **186**, 803–820 (2023).
38. Li, P. et al. Phase transitions in the assembly of multivalent signalling proteins. *Nature* **483**, 336–340 (2012).
39. Nott, T. J. et al. Phase transition of a disordered nuage protein generates environmentally responsive membraneless organelles. *Mol. Cell.* **57**, 936–947 (2015).
40. Zhang, Y. et al. Osmotic-induced reconfiguration and activation in membranized coacervate-based protocells. *J. Am. Chem. Soc.* **145**, 10396–10403 (2023).
41. Liu, W., Lupfer, C., Samanta, A., Sarkar, A. & Walther, A. Switchable hydrophobic pockets in DNA protocells enhance chemical conversion. *J. Am. Chem. Soc.* **145**, 7090–7094 (2023).
42. Erkamp, N. A. et al. Biomolecular condensates with complex architectures via controlled nucleation. *Nat. Chem. Eng.* **1**, 430–439 (2024).
43. Gobbo, P. et al. Catalytic processing in ruthenium-based polyoxometalate coacervate protocells. *Nat. Commun.* **11**, 41 (2020).
44. Yin, Y. et al. Non-equilibrium behaviour in coacervate-based protocells under electric-field-induced excitation. *Nat. Commun.* **7**, 10658 (2016).
45. Wang, X. et al. Synthetic-cell-based multi-compartmentalized hierarchical systems. *Small Methods* **7**, 2201712 (2023).
46. Zhu, M. et al. Tyrosine residues initiated photopolymerization in living organisms. *Nat. Commun.* **14**, 3598 (2023).
47. Lu, T., Chen, Q. & Liu, Z. A thorough theoretical exploration of intriguing characteristics of Cyclo[18]carbon: geometry, bonding nature, aromaticity, weak interaction, reactivity, excited states, vibrations, molecular dynamics and various molecular properties. Preprint at https://doi.org/10.26434/chemrxiv.11320130.v2, (2019).
48. Lu, T. & Chen, F. Multiwfn: A multifunctional wavefunction analyzer. *J. Comput. Chem.* **33**, 580–592 (2012).
49. Humphrey, W., Dalke, A. & Schulten, K. VMD: Visual molecular dynamics. *J. Mol. Graph.* **14**, 33–38 (1996).

Acknowledgements

We thank the National Natural Science Foundation of China (22377022, X. L.; 22475056, X. H.; and 22307030, H. C.), the Fundamental Research

Funds for the Central Universities (HIT.OCEF. 2023040) and China-German Mobility Program (M-0470) to X.H. for financial support.

Author contributions

M.Z. and X.H. conceived the project and designed the experiments; M.Z., Z.L. performed the experiments; M.Z., Z.L., J.L., Y.L., H.C., X.Q., X.W., X.L., X.H. undertook data analysis and discussed the results; M.Z., X.L. and X.H. wrote the manuscript.

Competing interests

The authors declare no competing interests.

Additional information

Supplementary information The online version contains supplementary material available at https://doi.org/10.1038/s41467-025-57069-1.

Correspondence and requests for materials should be addressed to Xiaoman Liu or Xin Huang.

Peer review information *Nature Communications* thanks Harsha Bajaj and the other, anonymous, reviewers for their contribution to the peer review of this work. A peer review file is available.